Use of X-ray computed tomography for studying the desiccation cracking and self-healing of fine soil during drying–wetting paths

Mohammed Zaidi, Nasre-Dine Ahfir, Abdellah Alem, Said Taibi, Bouabid El Mansouri, Yongxiang Zhang, Huaqing Wang

Use of X-ray computed tomography for studying the desiccation cracking and self-healing of fine soil during drying–wetting paths

Mohammed ZAIDI[1, 2], Nasre-Dine AHFIR[1*], Abdellah ALEM[1], Said TAIBI[1], Bouabid EL MANSOURI[2], Yongxiang ZHANG[3], Huaqing WANG[1,3]

[1]Normandie Univ., UNIHAVRE, UMR 6294 CNRS, LOMC, 76600 Le Havre, France.

[2]Laboratory of Geosciences of Natural Resources, Hydroinformatic section, Faculty of Sciences, Ibn Tofail University, Maamora Campus, BP.133, 14000 Kénitra, Morocco.

[3]Key Laboratory of Beijing for Water Quality Science and Water Environment Recovery Engineering, College of Architecture and Civil Engineering, Beijing University of Technology, Beijing 100124,

*Corresponding Author: Nasre-Dine AHFIR (ahfirn@univ-lehavre.fr)

Normandie Univ, UNIHAVRE, UMR 6294 CNRS, LOMC, 76600 Le Havre, France.

Phone number: +33 (0) 235-217-117, fax number: +33 (0) 235-217-198

Abstract

Managed aquifer recharge is an efficient approach using surface water for groundwater recharge. However, soil clogging in the infiltration systems represents a critical problem that reduces the efficiency of recharge systems. In recent years, much research has been conducted to investigate clogging in subsurface and surface soil (cake). Cake prevents infiltration into the water table and can drastically reduce the recharge rate. In arid and semi-arid areas, alternation of humid and dry seasons has an effect on cake cracking. In the present research, the propagation of desiccation cracking and self-healing of unconsolidated soil (cake), placed in Plexiglas columns, was investigated using X-ray computed tomography (CT) during drying–wetting (D-W) paths. The results showed that during the drying path, cracks initiated at the base of the soil by friction with the bottom of the column and then propagated to the top surface of the cake. As the drying time increased, evaporation at the top surface led to more cracks growing from the surface than from the bottom of the cake. However, the cracks at the bottom tended to stabilize because the water content was greater than at the top surface. The initiation, propagation, and expansion of the cracks developed in the saturated condition of the cake. During the wetting path, some cracks were closed while others appeared. The cracks tended to close progressively with wetting time, highlighting the self-healing phenomenon, probably due to the high plasticity index of cake soil. The results showed that cake swelling is mainly related to an increase of the void ratio due to a decrease in suction between particles. The results demonstrate the capacity of the X-ray CT technique to investigate the evolution of cracks during D-W paths.

Keywords: Soil cracking, Desiccation, Self-healing, Drying–wetting paths, Suction, X-ray computed tomography

1. Introduction

Climate change is a major global concern. Variations in seasonal meteorological conditions affect the water content of soils, especially in arid and semi-arid environments (Janetos et al., 1997; Komuscu et al., 1998; Longobardi, 2008; Wang et al., 2019). During dry periods, clay soils tend to deform and shrink (Pasricha et al., 2009; Tang et al., 2011a; Vogel et al., 2005). Shrinkage often leads to crack if the stresses, due to the prevented strain, are higher than the soil strength (Gribniak et al., 2007). Desiccation cracking modifies the mechanical properties (Tang et al., 2011b) and hydraulic properties (Albrecht and Benson, 2001; Chaduvula et al., 2007; Costa et al., 20013; Omidi et al., 1996; Rayhani et al., 2007) of the soil. In arid and semi-arid areas, which are characterized by high summer temperatures and overexploitation of water resources, managed aquifer recharge (MAR) remains an alternative solution that aims protects surface water (dams, rivers, etc.) from evaporation, by increasing the groundwater recharge from the surface and maintaining piezometric levels by injection into aquifer storage and recovery (ASR) wells, as well as by infiltration through infiltration basins, streambeds, etc. (Bouwer, 2002; Missimer et al., 2015). However, the rate of soil infiltration in MAR systems decreases over time due to the high sedimentation rate during recharge periods, dam releases, and/or flooding (Blaschke et al., 2003; Hatch et al., 2010; Rehg et al., 2005; Zaidi et al., 2020). This reduction in the infiltration rate occurs mainly at the surface of infiltration systems due to clogging of the porous medium by the deposited cake (Hutchison et al., 2013). In situ soils, in MAR facilities, are subject to diurnal changes and seasonal rainy and sunny weather, thus undergoing periodic drying-wetting cycles (Tang et al., 2011a). During dry periods, and for clayey soils, desiccation cracks considerably facilitate infiltration by creating rapid and deep percolation paths (Baram et al., 2012; Dunkerley, 2008; Topp and Davis, 1981) which in turn can contribute to groundwater recharge. The development of the desiccation crack is the result of the coupling between three factors: (i) the variation of the water content due to drying soil,

(ii) the stress equilibrium of deformation field corresponding to the inhomogeneous volume shrinkage, and (iii) the energy dissipation in the soil associated with the crack formation (An et al., 2020).

The shrinkage and desiccation cracks developed during dry periods in clays heal partially or completely during the subsequent wet periods (e.g. precipitation and recharge events), which is attributed to the self-healing property of clays (Leeds-Harrison et al., 1986; Cordero et al., 2014; Julina and Thyagaraj, 2020; Wang et al., 2017), leading to a decrease in hydraulic conductivity (Eigenbrod, 2003; Liu et al., 2003; Rayhani et al., 2008). Self-healing is an intrinsic behaviour in many nature's materials. For clayey soils, self-healing is mainly the result of soil swelling due to the presence of expanding clay minerals, i.e. smectite and montmorillonite (Favre et al., 1997), and/or the filling of cracks with solid particles or organic matter transported by flow (Joshi et al., 2017; Wang et al., 2014). Soil swelling and crack closure can be related to the increase in the void ratio as soil water content increases (Estabragh et al., 2013). A study conducted by Rayhani et al. (2008) on clay soils of different plasticity revealed that for highly plastic soils, hydraulic conductivity decreases with an increase in the plasticity index, during the wetting cycle. This behaviour can be explained by the self-healing of soil cracks after wetting. This result showed that self-healing occurs in highly plastic soils due to the high swelling potential of the soil, which allows open cracks to close, thereby reducing the hydraulic conductivity ratio. As a result, the hydraulic conductivity of highly plastic clay soils would no longer be controlled by the cracks that developed during drying. Eigenbrod (2003) explained the self-healing of cracks in fine-grained soils by three mechanisms: (i) an increase in effective stress above the undrained shear strength level of the intact soil; (ii) the sealing of fractures by eroded particles on the crack surfaces (suffusion) during percolation for non-plastic or low-plasticity soils; and (iii) the swelling of clay particles near the crack surfaces in highly swelling clays. Wang et al. (2018) showed that cracks perpendicular to the direction of infiltration block

continuous capillary flow as an air barrier that retards the infiltration compared to non-cracked soils, whereas longitudinal cracks (propagating in the direction of infiltration) serve as preferential flow paths and facilitate initial infiltration. The duration of preferential crack flow is controlled by the rate of swelling of the soil aggregates; this preferential flow becomes progressively slower as the cracks heal, due to the swelling dynamics of the soil matrix during the wetting process.

Most recent studies conducted on cracking are largely qualitative, based on observation tools such as digital cameras (Peron et al., 2009; Shokri et al., 2015; Tang et al., 2010), optical microscopes (Liang et al., 2019), and Scanning Electron Microscopy observations (Louati et al., 2018). To study the mechanisms of crack propagation inside the specimen, it becomes necessary to digitize the crack patterns and to make a quantitative assessment of the main crack characteristics such as geometric and micro-morphological parameters (e.g. crack area ratio, crack length, crack width, and crack depth). Thus, X-ray computed tomography (CT) imaging provides a powerful tool for identifying the nature and spatial configuration of soil components (Taina et al., 2008). X-ray CT allows accurate high-resolution visualization of the internal structure of specimens (Mees et al., 2003). Given the high contrast in the X-ray attenuation of soil cracks (or pores) and grains, their differentiation in X-ray CT is possible; which allows quantifying the geometrical and micro-morphological features of the cracks in three dimensions. Previous studies using X-ray CT to investigate the dynamics of desiccation cracking on compacted soils focused on the cracking process during drying without quantifying their closure following the wetting path (Julina and Thyagaraj, 2019; Tang et al., 2019).

This study continues the research carried out by Zaidi et al. (2020) related to evaluation of clogging of MAR in arid and semi-arid areas, as well as studying the effect of the presence of cracks in the cake on infiltration during dry seasons and post-wetting after rainfall. The objective of this study is to analyse the propagation of desiccation cracks using X-ray CT by

quantifying the geometrical parameters during drying–wetting (D-W) paths, in relation to the progressive 3D volume. For this purpose, crack propagation experiments were conducted on the cake during D-W paths. Also, this paper highlights the relationship between different parameters such as water content, void ratio, shrinkage, and swelling. Section 1 summarizes the state of the art. Section 2 presents the properties of the material, specimen preparation, and the research methodology. Section 3 discusses the results. Section 4 summarizes the major conclusions and points out future research directions.

2. Materials and methods

2.1. Soil properties

The Berrechid plain is located in the centre of Morocco (Fig. 1). It extends to 1500 km^2. This region is characterized by an arid to semi-arid climate, with an annual average temperature of 18 °C. The annual average rainfall varies from 280 to 310 mm/year (El Assaoui et al., 2015). As shown in Fig. 1, the aquifer's supply is mainly through direct rainfall infiltration and by wadi flows in the southern limit during flood events. El Himmer wadi extends 27 km in length, mainly supplied by flows from rainfall and releases from the dam upstream. This wadi has, since 2008, been equipped with a MAR system: two percolation tanks (S1 and S3) and two recharge releases (S2 and S4). After more than 10 years of use and despite some curing operations carried out to remove sediments transported by the flows, a high volume of these sediments settles along the wadi, particularly in percolation basins, thereby limiting groundwater recharge. A study conducted by Zaidi et al. (2020) showed that, despite the low rainfall (less than 1.4 mm/day) and short period (91 days) of the study, the deposit thickness exceeds 3 cm in a large part of the MAR. The hydraulic conductivity of the soil containing cracks, measured in situ during the drying period, ranged from 10^{-5} to 10^{-6} m/s, while the

hydraulic conductivity of the cake formed without cracks, measured in the laboratory, was 10^{-8} m/s.

Fig. 1

The soil used in the present study was collected from recharge site S1. Its properties are summarized in Table 1. According to the French standard for the classification of materials for earthworks, NF EN 16907–2 (2018), the soil of the cake is type F3-FH (High plasticity fine soil). The clayey fraction of the soil, analysed with the help of X-ray diffraction, is composed of vermiculite, interstratified illite-vermiculite, and two kaolinite polytypes (halloysite 7Å and dickite). The halloysite: dickite ratio was estimated using the RIR method as 15:2 (Zaidi et al., 2020). The physical properties of the soil, such as liquid limit w_L, plastic limit w_P, and plasticity index I_P were measured according to NF EN ISO 17892-12 (E) (2018).

Table 1

In order to characterize the sensitivity to soil dispersion due to wetting, three soil specimens were tested by the Crumb test method (ASTM D6572-20, 2020). The Crumb test was used to assess the reaction of the soil (dispersion) during the wetting phase. In this study, the Crumb test is used to evaluate the possibility of cracks filling with solid particles resulting from soil dispersion. The experimental process permits the temporal follow-up of the geometry of a centimetric dry specimen soil placed in distilled water without any external mechanical effort, and recording images of it over time. The tendency of soil particles to disperse in the colloidal suspension is estimated by observing the suspended cloud formed 2 min, 1 h, and 6 h after submerging. The results showed a partial collapse (disaggregation) after 2 min of hydration and total collapse after 1 h and 6 h, without observing dispersive particles, which can classify this soil as non-dispersive.

150 *2.2. Specimen preparation protocols*

151 The soil collected was oven-dried at 105 °C, crushed, and sieved through a 2 mm mesh
152 sieve. To obtain the cake specimen, dry soil was homogeneously mixed with water to reach an
153 initial water content of 200% corresponding to about three times the liquid limit. The water
154 content of 200% was chosen to obtain homogeneous liquid slurry allowing cake formation. The
155 liquid slurry was placed in Plexiglas columns of 50 mm inner diameter and 200 mm in height.
156 The final height of each prepared sample was about 180 mm. Porous caps and filter paper were
157 placed at the bottom of the columns to allow drainage. The surface was kept open to ensure
158 water evaporation at ambient temperature. A total of five specimens were prepared.

159

160 *2.3. Testing methods*

161 *2.3.1. Drying path*

162 The slurry specimens were kept in the laboratory to allow settling of the solid particles
163 by gravity to form the cake (to simulate in situ cake formation). Specimens were conserved
164 vertically under a constant temperature of 18.5 ± 0.5 °C. The surface layer of water (head) in
165 the columns partially infiltrated through the specimen; the rest evaporated. This stage of cake
166 formation took 3 weeks. Afterwards, the specimens were scanned by X-ray CT at different time
167 intervals. The specimens were scanned eight times, during 49 days of the drying path. The scans
168 were performed on the 4^{th}, 11^{th}, 18^{th}, 21^{st}, 29^{th}, 33^{rd}, 39^{th}, and 49^{th} days (Fig. 2). Also, the
169 samples were regularly weighed with a balance (accuracy of 0.001 g) to determine the
170 cumulative water loss and current total water content (w) of each specimen. The drying path
171 was stopped when w = 12%.

172

173

174

175 *2.3.2. Wetting path*

176 After the drying path, the specimens were immersed in water (from $w = 12\%$). Note that
177 the quantity of water used to immerse the specimens corresponds to the quantity necessary to
178 obtain a water content of $w = 100\%$ corresponding to $1.5w_L$. A syringe was used to fill the
179 columns carefully to avoid damaging the specimens. After that, the specimens were scanned
180 with X-ray CT after 24 h and 7 and 15 days of immersion (Fig. 2).

181 **Fig. 2**

182

183 *2.4. X-ray computed tomography*

184 The internal cracks formed during D-W paths were quantified using X-ray CT scanning
185 (Fig. 3) and image processing with ImageJ software (Fiji). This non-destructive technique
186 consists of measuring the progressive attenuation of X-rays due to absorption and scattering
187 when the beam traverses a material placed in its pathway. The X-ray CT technique produces
188 3D images of the X-ray absorption distribution in a specimen.

189 **Fig. 3**

190 X-ray scanning experiments were performed using an EasyTom 150 scanner (RX
191 Solutions, France) at the LOMC laboratory (University of Le Havre-Normandie). The scanner
192 was equipped with a 150 kV tungsten X-ray tube. In this study, samples were operated with an
193 accelerating voltage of 110 kV and a current of 376 µA. The data acquisition system recorded
194 1440 projections distributed over 360° along the vertical axis of the soil specimen with an
195 average of 10.5 images per second. The spatial resolution was 45 µm. Reconstruction of
196 projections was achieved with a cone-beam filtered back-projection algorithm (Feldkamp et al.,
197 1984) implemented in XAct software (RX Solutions) and the circular artefacts were attenuated
198 with a polynomial function for enhancing the image quality. 3D projections were reconstructed
199 from cross sections of horizontal and vertical planes.

200

201

202

203 *2.5. Image processing*

204 Image processing was performed using the open-source software ImageJ and a
205 collection of plugins included in Fiji (Schindelin et al., 2012). Several image processing
206 techniques were used to quantifying cracks propagation and soil structure (Chaduvula et al.,
207 2007; Lakshmikantha et al., 2009; Liu et al., 2011; Levatti el al., 2017).

208 As mentioned in section 2.3, eleven scans were performed during the D-W paths.
209 However, for the present paper, only five scans were selected based on the water content in
210 order to better represent the different D-W stages of the specimens. A total of 50 (± 3) slices
211 (2D) representing the horizontal cross sections of each specimen were chosen at equal distances
212 along the depth of the sample for further analysis. Sometimes, the contrast of an image was not
213 sufficient to view the image in detail. Therefore, the quality of the images was improved by
214 increasing the brightness and contrast, and a median filter with a radius of 2 voxels was then
215 applied to reduce noise in the images. A set scale was applied to all images based on the
216 resolution imposed during X-ray CT scanning (45 µm/pixel). The outline of the columns has
217 been removed to allow visualization of the specimens' volume in 3D as well as the distribution
218 and connectivity of deep cracks.

219 An image obtained by X-ray CT is a digital image of the grey values (matrix). The
220 histogram of the grey value distribution can be extracted from a reconstructed 3D volume. The
221 internal voids (cracks and pores) can be extracted when a suitable segmentation value is fixed
222 in this histogram by using the image thresholding technique (Duan et al., 2020). Many
223 thresholding approaches available in Fiji software were tested on all 3D images (stacks) to
224 identify a global representative threshold value. Most of each thresholding method was

validated by visually inspecting all the processed images. The majority of the methods provided good results for the images obtained during drying paths. However, for the wetting path images, and due to the presence of water in cracks, neither of the automatic methods showed acceptable results. Therefore, a manual thresholding method was chosen, by giving a set value for all images obtained during the drying path and a set value for images obtained during the wetting path.

2.6. Analysis of cracks

To quantify the variation of crack shape and change in specimen volume according to the water content during the D-W paths, the following parameters were calculated for each slice of X-ray CT images:

i. Specimen area

The specimen area represents the total area of the specimen.

ii. Crack ratio

The crack ratio is defined as the ratio between the surface area of the cracks and total area of the specimen (Peng et al., 2016; Zhang et al., 2013). This parameter reflects the extent of cracking in the soil.

iii. Average crack width and total crack length

Crack width is one of the important indices for characterizing the shape of a crack. It is closely related to crack propagation (Cheng et al., 2020). Crack width was calculated using the product of the distance map and the skeleton of the thresholded binary image (Fig. 4). The distance map shows for every pixel inside the crack the distance to its outer contour (edge of the crack). This distance has its maximum in the middle of the crack (Fig. 4c). This maximum value showed the distance from the mid-line to the edge of the crack. In other words, it represents the half-width of the crack. The maximum line can be obtained using the function Skeletonize.

250 However, the skeleton image showed only the position of the maximum line and did not contain
251 any distance information. That is why the skeleton image was changed to a binary image with
252 an intensity = 0 for the background and an intensity = 1 for the points of the line. Then, the
253 distance information in 'distance map image' was multiplied by the line position in 'skeleton
254 image'. All information about the maximum, the mean of the half-width of the crack, and the
255 crack length were obtained from the histogram image.
256 **Fig. 4**
257 To visualize the network of cracks in depth and the change in specimen volume during
258 the drying and wetting paths, 3D images were reconstructed from 2D projections using the
259 volume Viewer plugin available in ImageJ.
260
261 *2.7. Drying–wetting paths*
262 To highlight the shrinkage and swelling behaviour of the soil (cake), experiments on D-
263 W paths were carried out. The drying path consisted of imposing on the saturated slurry,
264 prepared with an initial water content equal to 1.3 times the liquid limit w_L, a series of increasing
265 suctions until reaching a dry state. The wetting path consisted of imposing on the dry soil a
266 series of decreasing suctions until quasi-saturation was achieved.
267 In order to sweep a wide range of suction pressure, two experimental techniques were
268 used: i) the osmotic control technique for suction varying from 50 kPa to 8 MPa, and ii) the
269 saturated salt solution technique for suction varying from 13 to 300 MPa. A brief description
270 of the theoretical principle of these two techniques is given by Blatz et al. (2008) and Fleureau
271 et al. (1993).
272 The osmotic technique is based on the use of semi-permeable membranes and an
273 aqueous solution of polyethylene glycol (PEG) organic molecules. Since water can pass through
274 the membrane, while PEG molecules in solution cannot because of their large size, a specimen

is brought into contact with a semi-permeable membrane behind which PEG solution flows subjected to osmotic suction. As the suction increases, PEG concentration also increases. Two PEG solutions, PEG 20,000 and PEG 6000, with an appropriate semi-permeable membrane, respectively SPECTRA/POR No. 4 and No. 3, were used (Kassiff and Ben, 1973; Zur, 1966).

The saturated salt solution technique that controls suction through the vapour phase is based on Kelvin's law relating the suction to the relative humidity. It consists of placing a sample in a confined atmosphere with controlled relative humidity in a desiccator and allowing water transfers in the vapour phase until equilibrium is reached. Relative humidity can be controlled using a given saturated salt solution (Blatz et al., 2008; Delage et al., 1998; Tang and Cui, 2005). In the present study, the saturated salt solutions used are summarized in Table 2.

Table 2

Once equilibrium was reached, the specimens were weighed and then were submerged in non-wetting oil (Commercial Kerdane) for a minimum of 2 h to fill the pores without swelling the specimens. The volume of the specimens was then determined from the difference between the weight after imbibition and the apparent weight when immersed in oil. Finally, the dry weight was obtained after evaporation of the oil and water at 105 °C for 24 h in an oven. Then, the void ratio (e), the degree of saturation (S_r), and the water content (w) were deduced.

3. Results and discussion

3.1. Shrinkage and swelling on drying–wetting paths

In this section, the behaviour of soils during D-W paths is analysed in order to highlight the shrinkage and swelling behaviour of the cake in relation to water content (w), suction (s), void ratio (e), and degree of saturation (S_r).

Fig. 5a shows the shrinkage curve in the [w, e] plane. On the drying path, the slurry first follows the saturation line ($e = \left(\frac{\gamma_s}{\gamma_w}\right) w$) as the water content decreases (γ_s is the solid bulk density and γ_w the water bulk density). The void ratio becomes quasi-constant when the water content reaches the shrinkage limit (w_{SL} = 20%) which is located at the intersection of the saturation line with the asymptote of the constant void ratio plateau. The wetting path, starting from zero water content, is overlaid with the drying path.

Fig. 5b presents the compressibility curve, i.e. variation of the void ratio as a function of the logarithm of suction [$log(s)$, e]. On the drying path, a change in void ratio results in a quasi-linear decrease in $log(s)$, corresponding to a normally consolidated compressibility path, to also reach a horizontal plateau. The intersection of drying and wetting paths defines the suction of shrinkage limit $s_{SL} = 10^4$ kPa and corresponds to stabilization of the void ratio. The wetting path from 296 MPa indicates quasi-reversibility of the drying path along this horizontal step until $s_{SL} = 10^4$ kPa. For suctions lower than s_{SL}, there is a hysteresis between the drying and wetting paths, due to the plastic strain undergone by the soil. As reported by Goh et al. (2014), under the same state of stress, a soil can behave differently during drying and wetting cycles because of hysteresis. The relationship between D-W paths and hysteresis cycle was discussed in detail by several authors (Auvray et al., 2004; Fleureau et al., 1993; Wang et al., 2017; Wheeler et al., 2003).

The evolution of the degree of saturation (S_r) as a function of water content (Fig. 5c) highlights the domain where S_r = 100%. When the water content decreases below the air entry point (w_{AE}), the degree of saturation drops significantly almost linearly with the water content, as long as the void ratio stays roughly constant (Fig. 5a). The air entry point (w_{AE} = 20%) is equal to the shrinkage limit (w_{SL} = 20%). Other researchers have reported this quasi-equality between w_{AE} and w_{SL} (Fleureau et al., 2002; Li et al., 2017).

322 Fig. 5d shows the variation in the degree of saturation (S_r) with suction ($log(s)$). The
323 cake remained saturated between 50 and 300 kPa, and the degree of saturation decreased to
324 about 5% when suction reached 296 MPa. It appears that the suction effect on the void ratio is
325 largely related to the saturation of the soil: the stage of maximum compressibility occurs when
326 the soil is practically saturated, whereas the void ratio becomes almost constant for a degree of
327 saturation below about 95%. The air-entry suction (s_{AE} =10^4 kPa) is roughly equal to the
328 shrinkage limit suction (s_{SL} = 10^4 kPa). Therefore, the shrinkage limit may be considered as the
329 transition point between the quasi-saturated and unsaturated domains.
330 Fig. 5e corresponds to the soil–water characteristic curve (SWCC). Changes in the water
331 content are mainly due to variations in the void ratio for suction below 10^4 kPa. Above this
332 value, the water content decreases significantly and a large reduction in the degree of saturation
333 leads to a drop in the water content of the soil below the shrinkage limit, with a corresponding
334 change in the slope of the curve. The wetting path in the [$log(s)$, w] plane shows hysteresis
335 when the suction is lower than the s_{SL} value, and is due to an increase in the void ratio (Fig. 5b)
336 and to the so-called 'ink bottle' phenomenon (Fleureau et al., 1993; Horgan and Ball, 2005).
337 **Fig. 5**
338 The analysis of the whole curves in Fig. 5 shows that the drainage path indicates two
339 fundamentally different phases: (i) the first one, where variations in the void ratio are important,
340 corresponds to a saturated state of the soil where water is continuous inside the sample and fills
341 the entire pore space. The effect of suction, in this case, is identical to the isotropic stress which
342 results in inclined contact forces that tend to rearrange the particles, causing plastic volume
343 variations. (ii) In the second part, where the void ratio is almost constant, the water is
344 discontinuous and localized at the points of contact between particles. The presence of the
345 meniscus generates forces normal to the tangent planes at the contacts that compress the
346 particles without causing a rearrangement of the particles, thus stopping the plastic volumetric

347 variation that reaches the shrinkage limit. From the shrinkage limit, the increase in capillary
348 pressure no longer affects the volume variations but continues to increase the contact forces
349 between particles, thus stiffening the soil.
350
351 *3.2. Crack propagation*

352 *3.2.1. Shrinkage and cracking during drying path*

353 A time series of 20 projections is shown in Fig. 6 to highlight the evolution of crack
354 propagation during the drying path as a function of water content. For clarity, only projections
355 for four water content (64%, 52%, 35%, and 12%) are presented. Also, the X-ray CT images
356 projected were chosen at 0% (top surface), 25%, 50%, 75%, and 100% depth (bottom surface).
357 The first crack appeared when the water content (w) decreased to 68% (noting that the liquid
358 limit, w_L = 66%). As shown in images corresponding to w = 64%, the first crack was initiated
359 at the bottom surface and then progressed inside the specimen. A second major crack
360 propagated laterally and joined the first crack, separating the specimen into two portions (cf.
361 images for w = 52% and w = 35%). With the continuing drying process, secondary cracks
362 appeared as ramifications of the major cracks, and propagated in different directions along the
363 primary crack (w = 35% and w = 12%). Cracks reached their maximum opening after 49 days
364 of drying, corresponding to a water content of 12%. Note that the initiation, propagation, and
365 expansion of the cracks developed in the saturated condition of the cake up to a water content
366 of about 20% (cf. Fig. 5c).

367 Drying resulted in an overall volumetric shrinkage, with a significant reduction in the
368 average height of the specimen from 44 to 36 mm between w = 64% and w = 12%, respectively.
369 As shown in Fig. 5a, void ratio becomes quasi-constant when the water content is less than
370 20%. That is why the drying process was stopped when the water content reached 12%.
371 **Fig. 6**

372

373 *3.2.2. Crack pattern evolution during wetting path*

374 Once the specimen reached w = 12%, it was wetted until w = 100%. To achieve that,
375 the specimen was submerged under a few centimetres of water head, simulating water loading
376 conditions in recharge sites. Three scans were performed during the wetting path: after 1, 7, and
377 15 days. Fig. 7a shows the morphology of the desiccation cracks in the dry state (w = 12%) with
378 the presence of two separate portions and a major open crack. After wetting, the small portion
379 of the specimen immediately collapsed (Fig. 7b). Fig. 7c and 7d represent the area of the non-
380 collapsed portion. Several factors may be responsible for specimen collapse (disaggregation)
381 associated with hydration, such as mineralogy, initial water content, wetting rate, and particle
382 size (Truman et al., 1990; Zhang and Norton, 2002). In the case of rapid wetting, which is the
383 case in the present study, differential swelling and air compression coupled with the weakening
384 of interparticle forces may cause aggregate failure (Grant and Dexter, 1990).

385 Desiccation cracks tend to close increasingly due to swelling of the specimen (Fig. 7b
386 and 7d). However, some new micro-cracks induced by wetting appeared after 24 h at the edges
387 of the major crack and the edges of the specimen (yellow and blue circles in Fig. 7d).
388 Differential swelling pressures and internal stresses during the wetting process are among the
389 main factors that cause these new cracks to appear. During drying process, the water contained
390 in the pores is replaced by air. The trapping and compression of air in the capillary openings
391 cause tensile forces. However, during wetting, the specimen adsorbs water, differential stresses
392 are created, causing weakness of specimen and the appearance of new cracks
393 (Doostmohammadi et al., 2009; Seedsman, 1993; Taylor and Spears, 1993).

394 **Fig. 7**

395 Fig. 8 shows images from the wetted specimen after 1, 7, and 15 days. The major crack
396 tended to close progressively with the wetting time. Also, the micro-cracks that appeared at the
397 edges of the specimen after 15 days of wetting were totally healed (Fig. 8c). As the clay

specimen was wetted, water infiltrated and penetrated the interparticle spaces, causing a decrease in suction between particles and resulting in progressive swelling of the specimen as shown on the wetting path in Fig. 5.

Fig. 8

To understand crack sealing following wetting processes, many studies have referred to the phenomenon of self-healing and its relationship to the physical parameters of soil particles. Rayhani et al. (2008) studied crack closure by measuring the permeability of soils of different plasticity index during the drying and wetting cycles. Their results showed that for some highly plastic soils, hydraulic conductivity decreases with an increase in permeation time, which is attributed to self-healing of the cracks. As reported by Cripps and Parmar (2015), although more cracks develop in high-plasticity clay soils, the self-healing phenomenon when the specimen is wetted is greater than in low-plasticity clays.

In the present study, the plasticity index I_p equals 34% (cf. Table 1). The crack closure, calculated from the average crack widths, indicates an average reduction of 38% between w = 12% (dry path) and w = 100% (after 15 days of wetting). Thus, the high plasticity index of the specimens tested in this study probably had a significant effect on the self-healing of the cracks.

3.3. Volume variation

Two-dimensional reconstructed projections were transformed to three dimensions to obtain a full 3D volume of the specimen. As indicated above (cf. section 3.2.2), only the large portion of the specimen remaining after wetting was retained for this analysis. Fig. 9 shows the variation in the volumetric deformation with D-W paths of the soil specimen (cake) at different water content (52%, 35%, 12%, and 100% after 24 h of wetting). It is clearly shown that the volumetric shrinkage of the cake was considerably accentuated during the drying path. The total

423 volume decreased from 56, 49, and 34 cm^3, respectively, for the water content of 52%, 35%,
424 and 12%. During the wetting path, the cake swelled up. The volume of the specimen was
425 increased by 41% after 15 days of wetting compared to the last scan at w = 12% (Fig. 10). In
426 the absence of expanding clay minerals such as smectite and montmorillonite in the studied
427 soil, swelling of the specimen was mainly related to an increase in the void ratio during wetting
428 due to the decrease in suction which attracted soil particles (Fig. 5a). The crack network
429 obtained from the 3D images provided a new insight into the appearance and development of
430 desiccation cracks in the cake, which was more interesting than the classical two-dimensional
431 analysis based on surface cracks only. It can also be mentioned that 90% of the specimen
432 swelling occurs after 24 h of wetting.

433 Usually, desiccation cracks are initiated at the top surface of the soil and continue to
434 progress inside the specimen (Julina and Thyagaraj, 2019; Tang et al., 2019). This is mainly
435 explained by the continuous removal of water from the surface by evaporation (Tran et al.,
436 2019; Wan et al., 2018) and tensile stress being at its maximum at the surface (Jenkins, 2005).
437 Furthermore, the formation and propagation of cracks are conditioned by (i) the evaporation
438 process governed by atmospheric conditions, (ii) the material properties, (iii) the specimen
439 dimensions (e.g. size, shape), (iv) and the existing or imposed physical boundary conditions
440 (An et al., 2020; Bažant, 1984; García-Álvarez, 1997; Gui and Zhao, 2015; Lakshmikantha et
441 al., 2012 & 2018; Lin el., 2020; Sánchez et al., 2014; Shit et al., 2015). The nominal strength
442 of geometrically similar structures can decrease with increasing size; and the crack patterns
443 may be controlled by the existing boundary conditions and the type of soil-boundary interface
444 (Lakshmikantha et al., 2012 & 2018).

445 In the present study, it is clearly shown from Fig. 9a and 9b that desiccation cracks are
446 initiated at depth and propagate upwards to the surface, even though the water content at the
447 bottom of the specimen is higher than that at the top surface. As mentioned in section 2.2, a

448 filter paper was placed at the bottom of each specimen, allowing drainage during the drying
449 path. This filter paper generated friction (stress concentration) with the bottom surface of the
450 specimen. This suggests that, although water evaporation begins at the exposed top surface,
451 cracks nucleate at the bottom due to friction between the specimen and the filter paper. This
452 behaviour has already been observed by Zeng et al. (2020).

453 Fig. 9c shows that when the water content reaches 12%, the development of lateral
454 cracks is observed. After wetting the specimen (Fig. 9d), these cracks opened significantly, and
455 others appeared. As mentioned above (section 3.2.2), the appearance of these new lateral cracks
456 is probably due to rapid hydration of the specimen, and the opening of pre-existing cracks is
457 due to the increase in the specimen volume. These new lateral cracks may not participate in
458 water infiltration because, as reported by Wang et al. (2018), cracks normal to the direction of
459 infiltration block continuous capillary flow, like an air barrier, and retard water infiltration,
460 whereas longitudinal cracks (propagating in the direction of infiltration) serve as preferential
461 flow paths and facilitate initial infiltration.

462 **Fig. 9**

463 **Fig. 10**

464

465 *3.4. Quantitative analysis of crack evolution*

466 A series of crack measurements were performed to assess the effects of D-W paths on
467 the development of cracks in the soil specimen (cake). The geometrical parameters used in the
468 analysis were introduced in section 2.6 (see also Fig. 4). The shrinkage of the cake, and the
469 crack network were analysed in terms of surface area change, crack ratio, total crack length,
470 and average crack width. This last parameter represents the average width measured along the
471 entire crack length. A detailed data of surface area change, crack ratio, total crack length, and
472 average crack width were presented in Table S1 and S2 in “Supplementary material”. As shown

473 in Fig. 11a, the surface area decreased with a decrease in water content. The decrease was 11%
474 for w = 35% and 37% for w = 12%, compared to the state at w = 52%. Therefore, in wet
475 conditions with w = 100%, the specimen swelled to reach, after 15 days of wetting, a surface
476 area close to that at w = 35%.

477 The crack ratio for different water contents revealed similar trends (Fig. 11b), increasing
478 with decreasing water content. Between 0 and 27 mm depth, the crack ratio is zero for w = 52%
479 because the cracks have not fully propagated to the top surface of the specimen (Fig. 9a).
480 Beyond this depth, the crack ratio curves change drastically due to damage of the cake at the
481 bottom. The crack ratio decreases after wetting the specimen and evolves in the same way as
482 during the drying path.

483 Fig. 11c and 11d show, as discussed in section 3.3. (Fig. 9a), that the cracks started at
484 the bottom and continued to propagate to the top surface of the specimen (cf. the curve for
485 w = 52%). During the drying path, for depth between 0 and 27 mm, opening of the desiccation
486 cracks increased with decreasing water content (Fig 11c) while, for depth between 27 and
487 45 mm, crack opening did not change much, particularly for w = 35% and w = 12%. This
488 behaviour can be explained by the difference in water content between the top and bottom of
489 each specimen tested in this study. In other words, during the drying path, crack width and
490 length are sensitive to the local water content (the specimen was drier on the top than on the
491 bottom). During the wetting process, the average crack width decreased over all depths of the
492 cake specimen (Fig. 11c). However, it was observed that the crack length increased (Fig. 11d)
493 after 1 day of wetting then decreased after 15 days. This increase in crack length can be
494 explained by the appearance of instantaneous new cracks due to rapid wetting of the specimen,
495 as discussed in sections 3.2.2 and 3.3. Between 1 and 15 days of wetting, the cake was swollen
496 and the cracks gradually shortened until reaching the same length as for w = 12%.

497 **Fig. 11**

4. Conclusion

A series of experimental investigations were conducted to study the cracking of the cake formed in MAR. Desiccation cracking and self-healing of the cake were analysed using X-ray CT during drying and wetting paths, respectively. An image processing technique was used to quantify the crack network and changes in cake volume. The results showed that, during the drying path, cracks were initiated at the base of the specimen due to friction with the bottom of the column, and then propagated to the top surface of the cake. As the drying time increased, evaporation at the top surface led to more cracks growing from the surface than from the bottom of the cake. However, the cracks in the cake bottom tended to stabilize because the water content was more important than at the top surface. The initiation, propagation, and expansion of the cracks developed in the saturated state of the cake.

During the wetting path, rapid wetting of the specimen generated lateral cracks and the vertical ones were partially closed. In the absence of expanding clay minerals such as smectite and montmorillonite in the studied soil, swelling of the specimen was mainly related to an increase in the void ratio due to the decrease in suction between particles. The cracks tended to close progressively with the wetting time, highlighting the self-healing phenomenon, probably due to the high plasticity index (34%) of the cake's soil.

The results presented in this investigation show that the cake formation in MAR, even after a period of dryness and therefore cracking, can have a harmful effect on water infiltration during wet periods. As shown in this study, after only 24 h of humidification, the cake swelled by almost 40% and crack openings were reduced by 38%. Considering the in situ factors present during wet periods, such as the contribution of fine particles deposited in these cracks and eventually cake collapse, it is probably that the infiltrability of these sites (MAR) will be greatly affected.

The results demonstrate the capacity of the X-ray CT technique to investigate the evolution of the cracks during D-W paths. However, to complete this study, further experiments are necessary, such as to increase the number of D-W cycles. Also, during wetting paths, it is important to evaluate the effect of water content at the beginning of the wetting process on cake self-healing.

Acknowledgment

This study is supported by PHC TOUBKAL project (18/74): Campus France N° 38951NJ.

References

Albrecht, B. A., & Benson, C. H., 2001. Effect of desiccation on compacted natural clays. Journal of Geotechnical and Geoenvironmental Engineering, 127(1), 67-75.

An, N., Tang, C. S., Cheng, Q., Wang, D. Y., & Shi, B., 2020. Application of electrical resistivity method in the characterization of 2D desiccation cracking process of clayey soil. Engineering Geology, 265, 105416

ASTM D6572 - 20, 2020. Test Methods for Determining Dispersive Characteristics of Clayey Soils by the Crumb Test. ASTM International. https://doi.org/10.1520/D6572-20

Auvray, R., Rosin-Paumier, S., Abdallah, A., & Masrouri, F., 2014. Quantification of soft soil cracking during suction cycles by image processing. European Journal of Environmental and Civil Engineering, 18(1), 11-32.

Baram, S., Kurtzman, D., Dahan, O., 2012. Water percolation through a clayey vadose zone. J. Hydrol. 424–425, 165–171. https://doi.org/10.1016/j.jhydrol.2011.12.040

Blaschke, A.P., Steiner, K.-H., Schmalfuss, R., Gutknecht, D., Sengschmitt, D., 2003. Clogging Processes in Hyporheic Interstices of an Impounded River, the Danube at Vienna, Austria. Int. Rev. Hydrobiol. 88, 397–413. https://doi.org/10.1002/iroh.200390034

Blatz, J.A., Cui, Y.-J., Oldecop, L., 2008. Vapour Equilibrium and Osmotic Technique for Suction Control. Geotech. Geol. Eng. 6, 661–673. https://doi.org/10.1007/s10706-008-9196-1

Bažant, Z. P., 1984. Size effect in blunt fracture: concrete, rock, metal. Journal of engineering mechanics, 110(4), 518-535.

Bouwer, H., 2002. Artificial recharge of groundwater: hydrogeology and engineering. Hydrogeol. J. 10, 121–142. https://doi.org/10.1007/s10040-001-0182-4

555 Chaduvula, U., Viswanadham, B. V. S., & Kodikara, J., 2017. A study on desiccation cracking behavior of
556 polyester fiber-reinforced expansive clay. Applied Clay Science, 142, 163-172.

557 Cheng, Q., Tang, C.-S., Zeng, H., Zhu, C., An, N., Shi, B., 2020. Effects of microstructure on desiccation
558 cracking of a compacted soil. Eng. Geol. 265, 105418.
559 https://doi.org/10.1016/j.enggeo.2019.105418

560 Cripps, J.C., Parmar, K.K., 2015. Investigations into the Self-Healing of Desiccation Cracks in Compacted
561 Clays, in: Lollino, G., Manconi, A., Guzzetti, F., Culshaw, M., Bobrowsky, P., Luino, F. (Eds.),
562 Engineering Geology for Society and Territory - Volume 5. Springer International Publishing,
563 Cham, pp. 1327–1331. https://doi.org/10.1007/978-3-319-09048-1_253

564 Cordero, J., Cuadrado, A., Ledesma, A. and Prat, P.C. 2014. Patterns of cracking in soils due to drying and
565 wetting cycles. In 6th International Conference on Unsaturated Soils (UNSAT 2014). Edited by N.
566 Khalili, A. Russell and A. Khoshghalb, Sydney, Australia, 2-4 July. Taylor and Francis, pp. 381-
567 387.

568 Costa, S., Kodikara, J. K., & Shannon, B., 2013. Salient factors controlling desiccation cracking of clay in
569 laboratory experiments. Géotechnique, 63(1), 18-29.

570 Delage, P., Howat, M.D., Cui, Y.J., 1998. The relationship between suction and swelling properties in a
571 heavily compacted unsaturated clay. Eng. Geol. 50, 31–48. https://doi.org/10.1016/S0013-
572 7952(97)00083-5

573 Doostmohammadi, R., Moosavi, M., Mutschler, T., & Osan, C., 2009. Influence of cyclic wetting and drying
574 on swelling behavior of mudstone in south west of Iran. Environmental Geology, 58(5), 999.
575 https://doi.org/10.1007/s00254-008-1579-3

576 Duan, Y.T., Li, X., Ranjith, P.G., Wu, Y.F., 2020. An investigation of the evolution of the internal
577 structures and failure modes of Longmaxi shale using novel X-ray microscopy. J. Pet. Sci. Eng.
578 184, 106479. https://doi.org/10.1016/j.petrol.2019.106479

579 Dunkerley, D.L., 2008. Bank permeability in an Australian ephemeral dry-land stream: variation with stage
580 resulting from mud deposition and sediment clogging. Earth Surf. Process. Landf. 33, 226–243.
581 https://doi.org/10.1002/esp.1539

582 Eigenbrod, K.D., 2003. Self-healing in fractured fine-grained soils. Can. Geotech. J. 40, 435–449.
583 https://doi.org/10.1139/t02-110

584 El Assaoui, N., Amraoui, F., El Mansouri, B., 2015. Modeling of Climate Changes Impact on Groundwater
585 Resources of Berrechid Aquifer 4, 15. https://doi.org/10.15680/IJIRSET.2015.0407118

586 Estabragh, A.R., Moghadas, M., Javadi, A.A., 2013. Effect of different types of wetting fluids on the
587 behaviour of expansive soil during wetting and drying. Soils Found. 53, 617–627.
588 https://doi.org/10.1016/j.sandf.2013.08.001

589 Favre, F., Boivin, P., Wopereis, M.C.S., 1997. Water movement and soil swelling in a dry, cracked
590 Vertisol. Geoderma 78, 113–123. https://doi.org/10.1016/S0016-7061(97)00030-X

591 Feldkamp, L.A., Davis, L.C., Kress, J.W., 1984. Practical cone-beam algorithm. J Opt Soc Am 612–619.

592 Fleureau, J.-M., Kheirbek-Saoud, S., Soemitro, R., Taibi, S., 1993. Behavior of clayey soils on drying–
593 wetting paths. Can. Geotech. J. 30, 287–296. https://doi.org/10.1139/t93-024

Fleureau, J.-M., Verbrugge, J.-C., Huergo, P.J., Correia, A.G., Kheirbek-Saoud, S., 2002. Aspects of the behaviour of compacted clayey soils on drying and wetting paths 39, 17.

Goh, S. G., Rahardjo, H., & Leong, E. C., 2014. Shear strength of unsaturated soils under multiple drying-wetting cycles. Journal of Geotechnical and Geoenvironmental Engineering, 140(2), 06013001.

Grant, C.D., Dexter, A.R., 1990. Air entrapment and differential swelling as factors in the mellowing of molded soil during rapid wetting. Soil Res. 28, 361–369. https://doi.org/10.1071/sr9900361

Gribniak, V., Kaklauskas, G., Baèinskas, D., 2007. State-of-art review of shrinkage effect on cracking and deformations of concrete bridge elements. Balt. J. ROAD BRIDGE Eng. 12.

Gui, Y., and Zhao, G. F., 2015, "Modelling of laboratory soil desiccation cracking using DLSM with a two-phase bond model," Computers and Geotechnics, Vol. 69, pp. 578-587.

Hatch, C.E., Fisher, A.T., Ruehl, C.R., Stemler, G., 2010. Spatial and temporal variations in streambed hydraulic conductivity quantified with time-series thermal methods. J. Hydrol. 389, 276–288. https://doi.org/10.1016/j.jhydrol.2010.05.046

Horgan, G. W., and Ball, B. C., 2005. Modelling the effect of water distribution and hysteresis on air-filled pore space. European journal of soil science, 56(5), 647-654.

Hutchison, A., Milczarek, M., Banerjee, M., 2013. Clogging Phenomena Related to Surface Water Recharge Facilities, in: Clogging Issues Associated with Managed Aquifer Recharge Methods. Australia, p. 25.

Janetos, A.C., Watson, R.T., Zinyowera, M.C., Moss, R.H., 1997. Climate Change 1995: Impacts, Adaptations and Mitigation of Climate Change: Scientific-Technical Analyses. Ecology 78, 2644. https://doi.org/10.2307/2265930

Jenkins, D.R., 2005. Optimal spacing and penetration of cracks in a shrinking slab. Phys. Rev. E 71, 056117. https://doi.org/10.1103/PhysRevE.71.056117

Joshi, S., Goyal, S., Mukherjee, A., Reddy, M.S., 2017. Microbial healing of cracks in concrete: a review. J. Ind. Microbiol. Biotechnol. 44, 1511–1525. https://doi.org/10.1007/s10295-017-1978-0

Julina, M., Thyagaraj, T., 2019. Quantification of desiccation cracks using X-ray tomography for tracing shrinkage path of compacted expansive soil. Acta Geotech. 14, 35–56. https://doi.org/10.1007/s11440-018-0647-4

Julina, M., & Thyagaraj, T., 2020. Combined effects of wet-dry cycles and interacting fluid on desiccation cracks and hydraulic conductivity of compacted clay. Engineering Geology, 267, 105505.

Kassiff, G., Ben, S., A., 1973. Discussion: Experimental relationship between swell pressure and suction. Géotechnique 23, 125–127. https://doi.org/10.1680/geot.1973.23.1.125

Komuscu, A.U., Erkan, A., Oz, S., 1998. Possible Impacts of Climate Change on Soil Moisture Availability in the Southeast Anatolia Development Project Region (GAP): An Analysis from an Agricultural Drought Perspective. Clim. Change 40, 519–545. https://doi.org/10.1023/A:1005349408201

Lakshmikantha, M. R., Prat, P. C., and Ledesma, A., 2009, "Image analysis for the quantification of a developing crack network on a drying soil," Geotechnical Testing Journal, Vol. 32, No. 6, pp. 505-515.

631 Lakshmikantha, M. R., Prat, P. C., & Ledesma, A., 2012. Experimental evidence of size effect in soil
632 cracking. Canadian Geotechnical Journal, 49(3), 264-284.

633 Lakshmikantha, M. R., Prat, P. C., & Ledesma, A., 2018. Boundary effects in the desiccation of soil layers
634 with controlled environmental conditions. Geotechnical Testing Journal, 41(4), 675-697.

635 Levatti, H.U., Prat, P.C., Ledesma, A., Cuadrado, A. and Cordero, J.A. 2017. Experimental analysis of 3D
636 cracking in drying soils using Ground Penetrating Radar. Geotechnical Testing Journal 40(2):221-
637 243.

638 Leeds-Harrison, P.B., Shipway, C.J.P., Jarvis, N.J., Youngs, E.G., 1986. The influence of soil macroporosity
639 on water retention, transmission and drainage in a clay soil. Soil Use Manag. 2, 47–50.
640 https://doi.org/10.1111/j.1475-2743.1986.tb00678.x

641 Li, Z.-S., Fleureau, J.-M., Tang, L.-S., 2017. Aspects of compaction and drying–wetting curves of a
642 subgrade clayey soil. Géotechnique 1–7. https://doi.org/10.1680/jgeot.16.T.010

643 Liang, C., Gui, Y., van der Land, C., 2019. Microscope observation of cracks of clay. E3S Web Conf. 92,
644 03007. https://doi.org/10.1051/e3sconf/20199203007

645 Lin, Z. Y., Wang, Y. S., Tang, C. S., Cheng, Q., Zeng, H., Liu, C., & Shi, B., 2021. Discrete element
646 modelling of desiccation cracking in thin clay layer under different basal boundary
647 conditions. Computers and Geotechnics, 130, 103931.

648 Liu, C.-W., Cheng, S.-W., Yu, W.-S., Chen, S.-K., 2003. Water infiltration rate in cracked paddy soil.
649 Geoderma 117, 169–181. https://doi.org/10.1016/S0016-7061(03)00165-4

650 Liu, C., Shi, B., Zhou, J., and Tang, C.-S., 2011, "Quantification and characterization of microporosity by
651 image processing, geometric measurement and statistical methods: Application on SEM images of
652 clay materials," Applied Clay Science, Vol. 54, No. 1, pp. 97-106.

653 Longobardi, A., 2008. Observing soil moisture temporal variability under fluctuating climatic conditions.
654 Hydrol. Earth Syst. Sci. Discuss. 5, 935–969.

655 Louati, F., Trabelsi, H., Jamei, M., Taibi, S., 2018. Impact of wetting-drying cycles and cracks on the
656 permeability of compacted clayey soil. Eur. J. Environ. Civ. Eng. 0, 1–26.
657 https://doi.org/10.1080/19648189.2018.1541144

658 Mees, F., Swennen, R., Geet, M.V., Jacobs, P., 2003. Applications of X-ray computed tomography in the
659 geosciences. Geol. Soc. Lond. Spec. Publ. 215, 1–6.
660 https://doi.org/10.1144/GSL.SP.2003.215.01.01

661 Missimer, T.M., Guo, W., Maliva, R.G., Rosas, J., Jadoon, K.Z., 2015. Enhancement of wadi recharge
662 using dams coupled with aquifer storage and recovery wells. Environ. Earth Sci. 73, 7723–7731.
663 https://doi.org/10.1007/s12665-014-3410-7

664 NF EN ISO 17892-12 (E), 2018. Geotechnical investigation and testing - Laboratory testing of soil - Part
665 12: Determination of liquid and plastic limits.

666 NF EN 16907-2 (2018) : Earthworks - Part 2 : classification of materials

667 Omidi, G.H., Thomas, J.C., Brown, K.W., 1996. Effect of desiccation cracking on the hydraulic conductivity
668 of a compacted clay liner. Water. Air. Soil Pollut. 89, 91–103. https://doi.org/10.1007/BF00300424

669 Pasricha, K., Wad, U., Pasricha, R., Ogale, S., 2009. Parametric dependence studies on cracking of clay.
670 Phys. Stat. Mech. Its Appl. 388, 1352–1358. https://doi.org/10.1016/j.physa.2008.12.039

671 Peng, X., Zhang, Z.B., Gan, L., Yoshida, S., 2016. Linking Soil Shrinkage Behavior and Cracking in Two
672 Paddy Soils as Affected by Wetting and Drying Cycles. Soil Sci. Soc. Am. J. 80, 1145–1156.
673 https://doi.org/10.2136/sssaj2015.07.0273

674 Peron, H., Hueckel, T., Laloui, L., and Hu, L. B., 2009, "Fundamentals of desiccation cracking of fine-grained
675 soils: experimental characterisation and mechanisms identification," Canadian Geotechnical Journal,
676 Vol. 46, No. 10, pp. 1177-1201.

677 Rayhani, M.H., Yanful, E.K., Fakher, A., 2007. Desiccation-induced cracking and its effect on the
678 hydraulic conductivity of clayey soils from Iran. Can. Geotech. J. 44, 276–283.
679 https://doi.org/10.1139/t06-125

680 Rayhani, M.H.T., Yanful, E.K., Fakher, A., 2008. Physical modeling of desiccation cracking in plastic
681 soils. Eng. Geol. 97, 25–31. https://doi.org/10.1016/j.enggeo.2007.11.003

682 Rehg, K.J., Packman, A.I., Ren, J., 2005. Effects of suspended sediment characteristics and bed sediment
683 transport on streambed clogging. Hydrol. Process. 19, 413–427. https://doi.org/10.1002/hyp.5540

684 Sánchez, M., Manzoli, O. L., and Guimarães, L. N., 2014, "Modeling 3-D desiccation soil crack networks
685 using a mesh fragmentation technique," Computers and Geotechnics, Vol. 62, pp. 27-39.

686 Schindelin, J., Arganda-Carreras, I., Frise, E., Kaynig, V., Longair, M., Pietzsch, T., Preibisch, S., Rueden,
687 C., Saalfeld, S., Schmid, B., Tinevez, J.-Y., White, D.J., Hartenstein, V., Eliceiri, K., Tomancak,
688 P., Cardona, A., 2012. Fiji: an open-source platform for biological-image analysis. Nat. Methods 9,
689 676–682. https://doi.org/10.1038/nmeth.2019

690 Seedsman, R. W., 1993. Characterizing clay shales. In Rock Testing and Site Characterization (pp. 151-
691 165). Pergamon.

692 Shit, P. K., Bhunia, G. S., and Maiti, R., 2015, "Soil crack morphology analysis using image processing
693 techniques," Modeling Earth Systems and Environment, Vol. 1, No. 4, pp. 1-7.

694 Shokri, N., Zhou, P., Keshmiri, A., 2015. Patterns of Desiccation Cracks in Saline Bentonite Layers.
695 Transp. Porous Media 110, 333–344. https://doi.org/10.1007/s11242-015-0521-x

696 Taina, I. A., Heck, R. J., & Elliot, T. R., 2008. Application of X-ray computed tomography to soil science:
697 A literature review. Canadian Journal of Soil Science, 88(1), 1-19.

698 Tang, A.-M., Cui, Y.-J., 2005. Controlling suction by the vapour equilibrium technique at different
699 temperatures and its application in determining the water retention properties of MX80 clay. Can.
700 Geotech. J. 42, 287–296. https://doi.org/10.1139/t04-082

701 Tang, C.-S., Cui, Y.-J., Shi, B., Tang, A.-M., Liu, C., 2011a. Desiccation and cracking behaviour of clay
702 layer from slurry state under wetting–drying cycles. Geoderma 166, 111–118.
703 https://doi.org/10.1016/j.geoderma.2011.07.018

704 Tang, C.-S., Cui, Y.-J., Tang, A.-M., Shi, B., 2010. Experiment evidence on the temperature dependence of
705 desiccation cracking behavior of clayey soils. Eng. Geol. 114, 261–266.
706 https://doi.org/10.1016/j.enggeo.2010.05.003

Tang, C.-S., Shi, B., Liu, C., Suo, W.-B., Gao, L., 2011b. Experimental characterization of shrinkage and desiccation cracking in thin clay layer. Appl. Clay Sci. 52, 69–77. https://doi.org/10.1016/j.clay.2011.01.032

Tang, C.-S., Zhu, C., Leng, T., Shi, B., Cheng, Q., Zeng, H., 2019. Three-dimensional characterization of desiccation cracking behavior of compacted clayey soil using X-ray computed tomography. Eng. Geol. 255, 1–10. https://doi.org/10.1016/j.enggeo.2019.04.014

Taylor, R. K., & Spears, D. A., 1970. The breakdown of British coal measure rocks. In International Journal of Rock Mechanics and Mining Sciences & Geomechanics Abstracts (Vol. 7, No. 5, pp. 481-501). Pergamon.

Topp, G.C., Davis, J.L., 1981. Detecting infiltration of water through soil cracks by time-domain reflectometry. Geoderma 26, 13–23. https://doi.org/10.1016/0016-7061(81)90073-2

Tran, D.K., Ralaizafisoloarivony, N., Charlier, R., Mercatoris, B., Léonard, A., Toye, D., Degré, A., 2019. Studying the effect of desiccation cracking on the evaporation process of a Luvisol – From a small-scale experimental and numerical approach. Soil Tillage Res. 193, 142–152. https://doi.org/10.1016/j.still.2019.05.018

Truman, C.C., Bradford, J.M., Ferris, J.E., 1990. Antecedent Water Content and Rainfall Energy Influence on Soil Aggregate Breakdown. Soil Sci. Soc. Am. J. 54, 1385–1392. https://doi.org/10.2136/sssaj1990.03615995005400050030x

Vogel, H.-J., Hoffmann, H., Leopold, A., Roth, K., 2005. Studies of crack dynamics in clay soil: II. A physically based model for crack formation. Geoderma 125, 213–223. https://doi.org/10.1016/j.geoderma.2004.07.008

Wan, Y., Xue, Q., Liu, L., Wang, S., 2018. Relationship between the shrinkage crack characteristics and the water content gradient of compacted clay liner in a landfill final cover. Soils Found. 58, 1435–1445. https://doi.org/10.1016/j.sandf.2018.08.011

Wang, C., Zhang, Z., Fan, S., Mwiya, R., Xie, M., 2018. Effects of straw incorporation on desiccation cracking patterns and horizontal flow in cracked clay loam. Soil Tillage Res. 182, 130–143. https://doi.org/10.1016/j.still.2018.04.006

Wang, C., Zhang, Z., Liu, Y., Fan, S., 2017. Geometric and fractal analysis of dynamic cracking patterns subjected to wetting-drying cycles. Soil Tillage Res. 170, 1–13. https://doi.org/10.1016/j.still.2017.02.005

Wang, J., Dewanckele, J., Cnudde, V., Van Vlierberghe, S., Verstraete, W., De Belie, N., 2014. X-ray computed tomography proof of bacterial-based self-healing in concrete. Cem. Concr. Compos. 53, 289–304. https://doi.org/10.1016/j.cemconcomp.2014.07.014

Wang, Y., Yang, J., Chen, Y., Fang, G., Duan, W., Li, Y., De Maeyer, P., 2019. Quantifying the Effects of Climate and Vegetation on Soil Moisture in an Arid Area, China. Water 11, 767. https://doi.org/10.3390/w11040767

Wheeler, S. J., Sharma, R. S., & Buisson, M. S. R., 2003. Coupling of hydraulic hysteresis and stress–strain behaviour in unsaturated soils. Géotechnique, 53(1), 41-54.

745 Zaidi, M., Ahfir, N.-D., Alem, A., El Mansouri, B., Wang, H., Taibi, S., Duchemin, B., Merzouk, A., 2020.
746 Assessment of clogging of managed aquifer recharge in a semi-arid region. Sci. Total Environ.
747 730, 139107. https://doi.org/10.1016/j.scitotenv.2020.139107

748 Zeng, H., Tang, C.-S., Cheng, Q., Zhu, C., Yin, L.-Y., Shi, B., 2020. Drought-Induced Soil Desiccation
749 Cracking Behavior With Consideration of Basal Friction and Layer Thickness. Water Resour. Res.
750 56, e2019WR026948. https://doi.org/10.1029/2019WR026948

751 Zhang, X.C., Norton, L.D., 2002. Effect of exchangeable Mg on saturated hydraulic conductivity,
752 disaggregation and clay dispersion of disturbed soils. J. Hydrol. 260, 194–205.
753 https://doi.org/10.1016/S0022-1694(01)00612-6

754 Zhang, Z.B., Peng, X., Wang, L.L., Zhao, Q.G., Lin, H., 2013. Temporal changes in shrinkage behavior of
755 two paddy soils under alternative flooding and drying cycles and its consequence on percolation.
756 Geoderma 192, 12–20. https://doi.org/10.1016/j.geoderma.2012.08.009

757 Zur, B., 1966. Osmotic control of the matric soil-water potential: I. soil-water system. Soil Sci. 102, 394–
758 398.

Figures

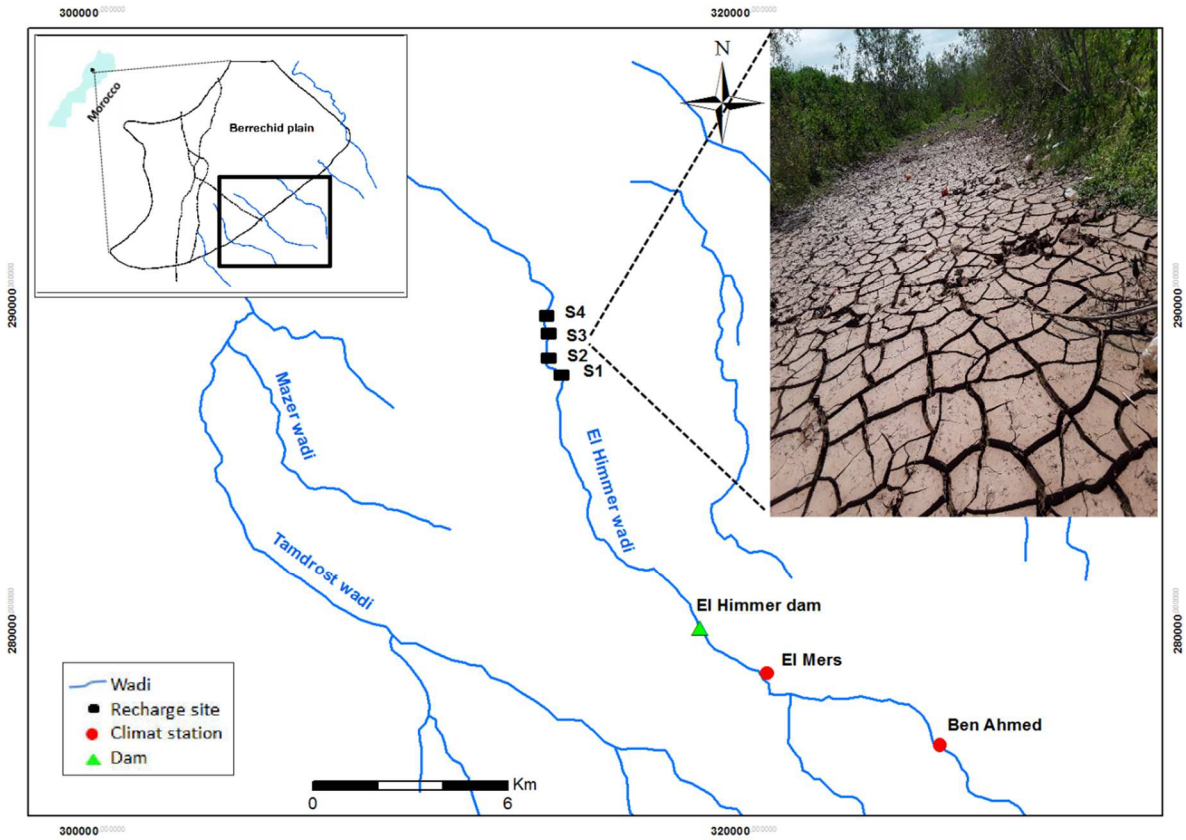

Fig. 1. Managed aquifer recharge sites located along El Himmer wadi. Inset photo indicates the desiccation cracks of the cake formed in the wadi bed

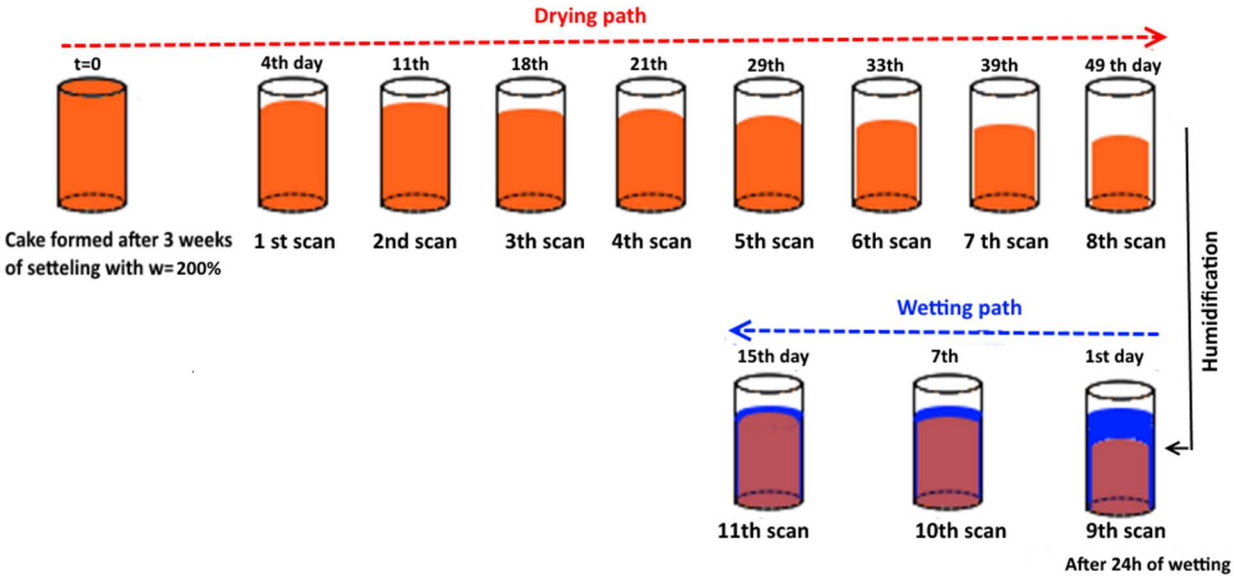

Fig. 2. Schematic drawing of D-W paths applied to the specimens

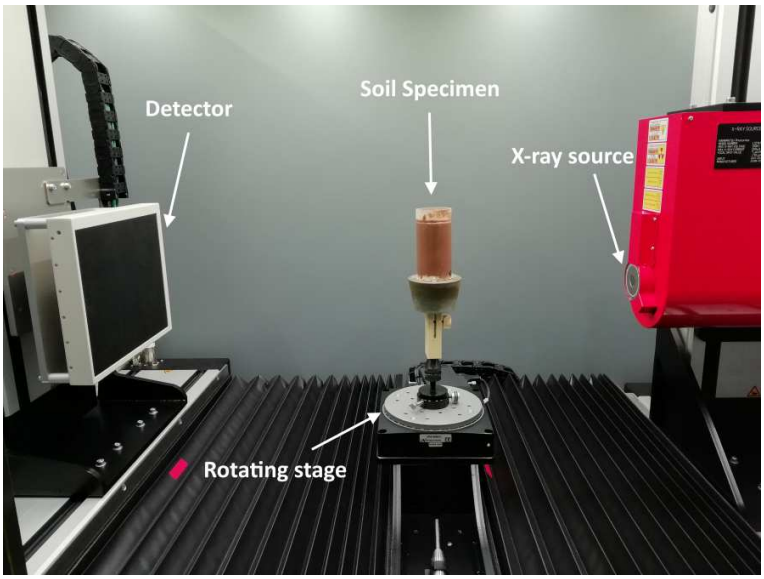

Fig. 3. Inner view of the X-ray tomography scanner used in this study

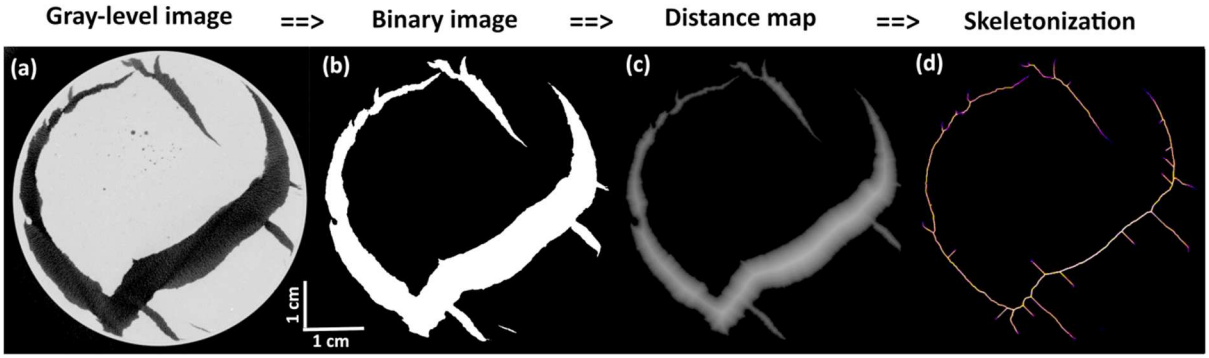

Fig. 4. Procedure of CT images processing, (a) original CT image, (b) binary image, (c) maximum distance, and (d) crack skeleton

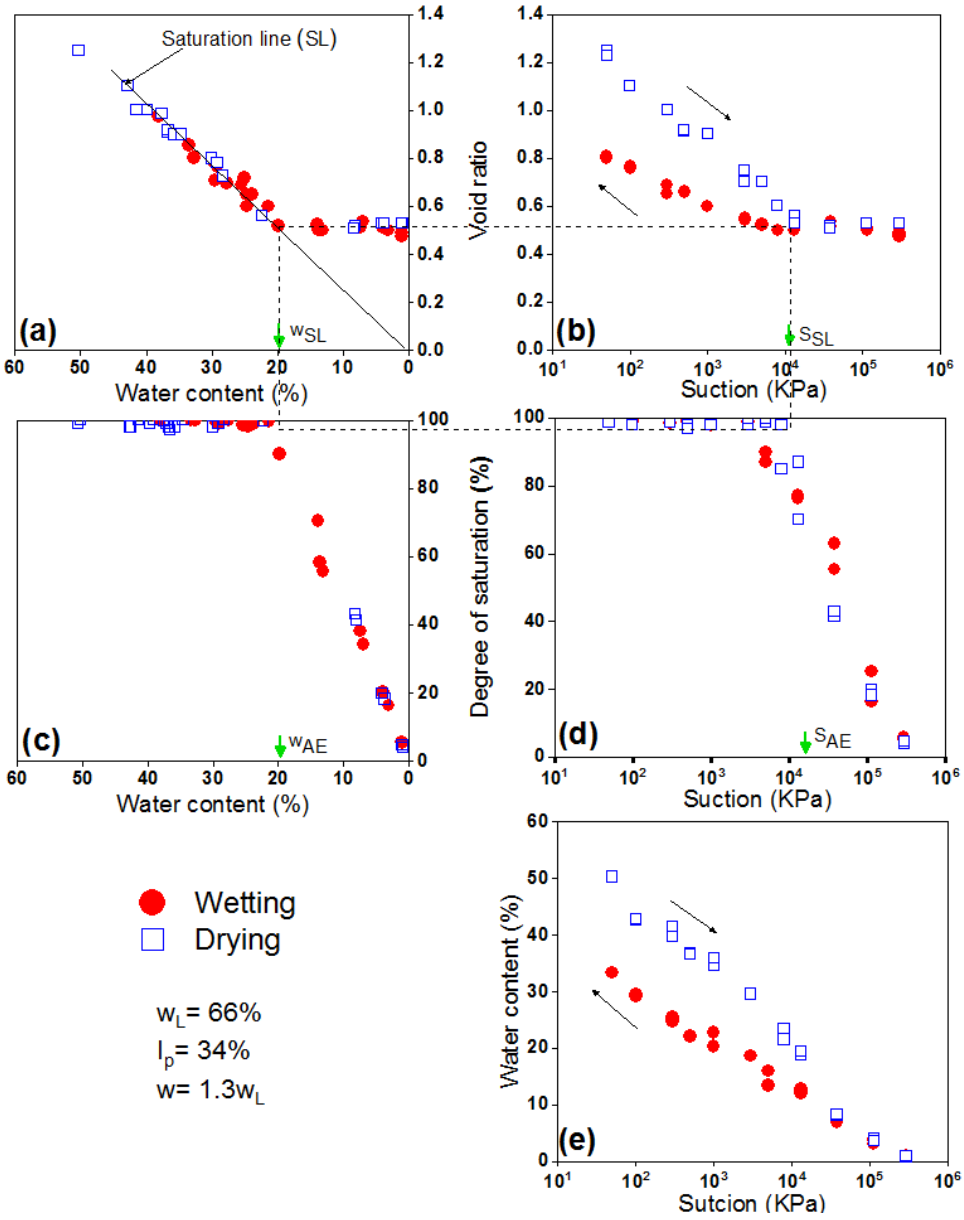

Fig. 5. Synthesis of drying-wetting paths of the cake

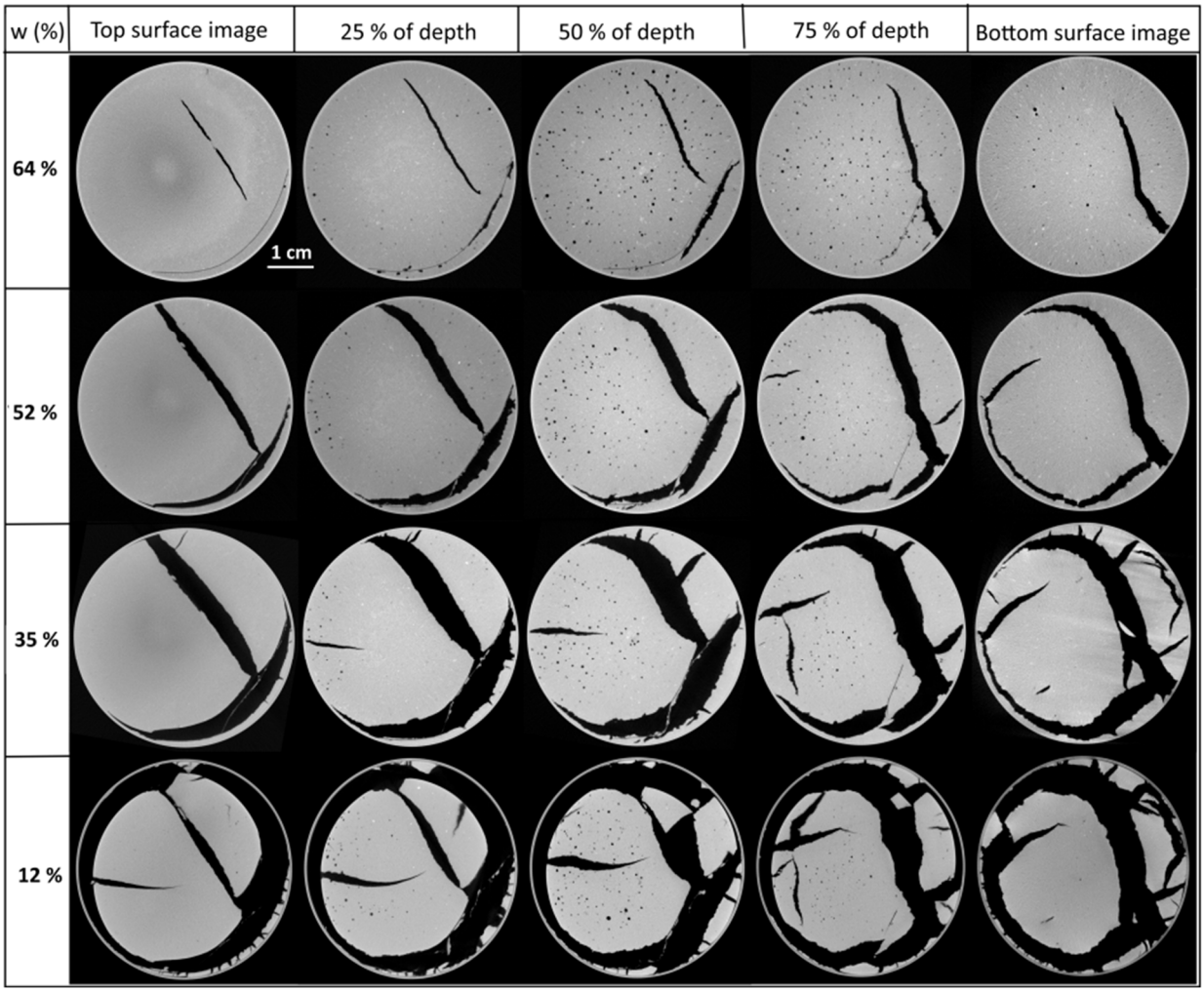

Fig. 6. X-ray CT scan of horizontal cracking pattern during dying path at different depths of the specimen for different water content

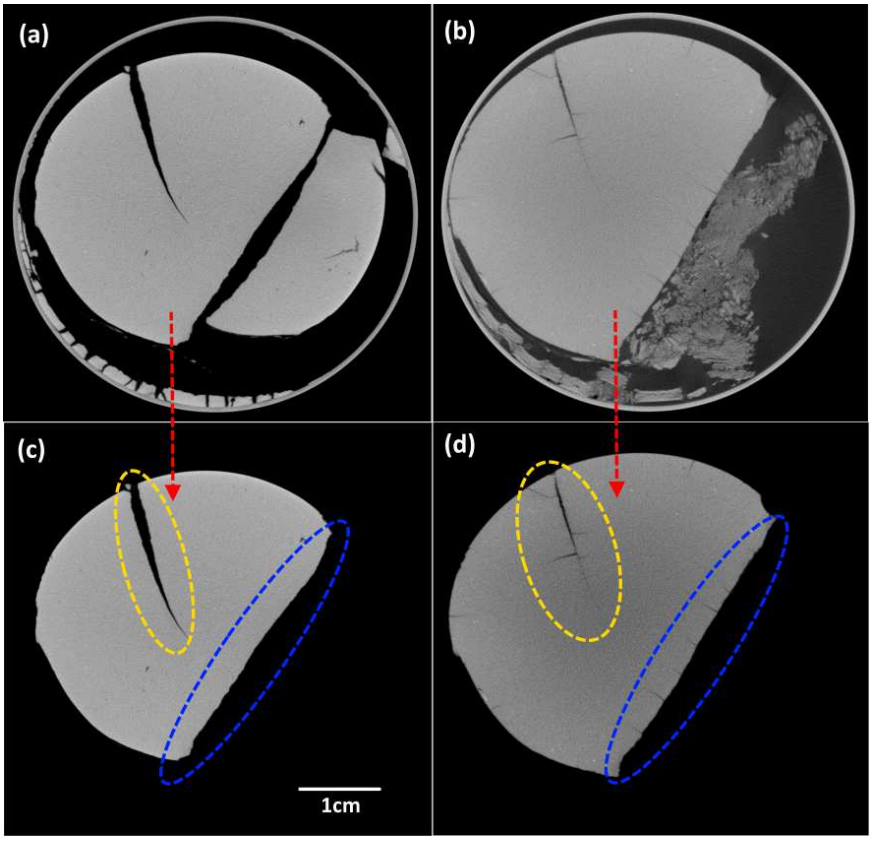

Fig. 7. Image of cracks (a) at w=12%, and (b) after 24h wetting. Images (c) and (d) represent the area of the non-collapsed portion

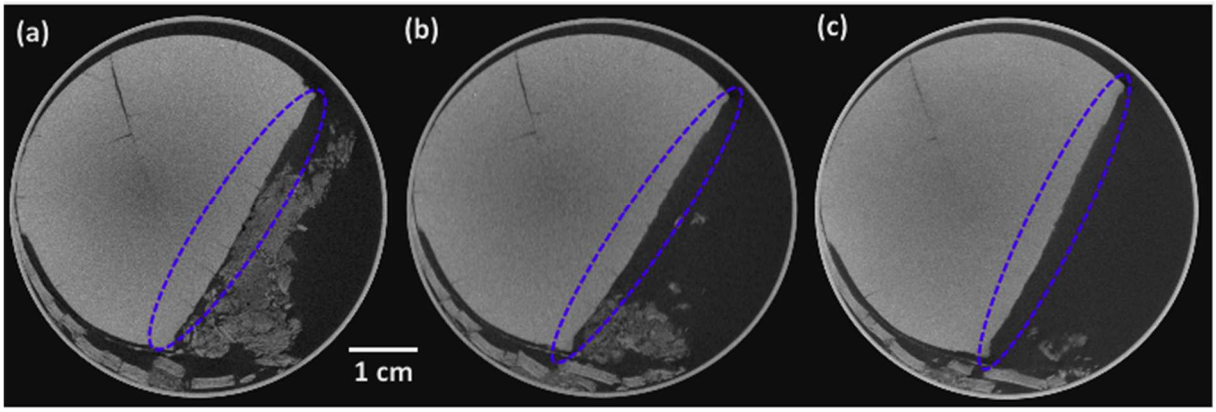

Fig. 8. Evolution of crack healing during the wetting path after (a) 24 hours, (b) 7 days, and (d) 15 days

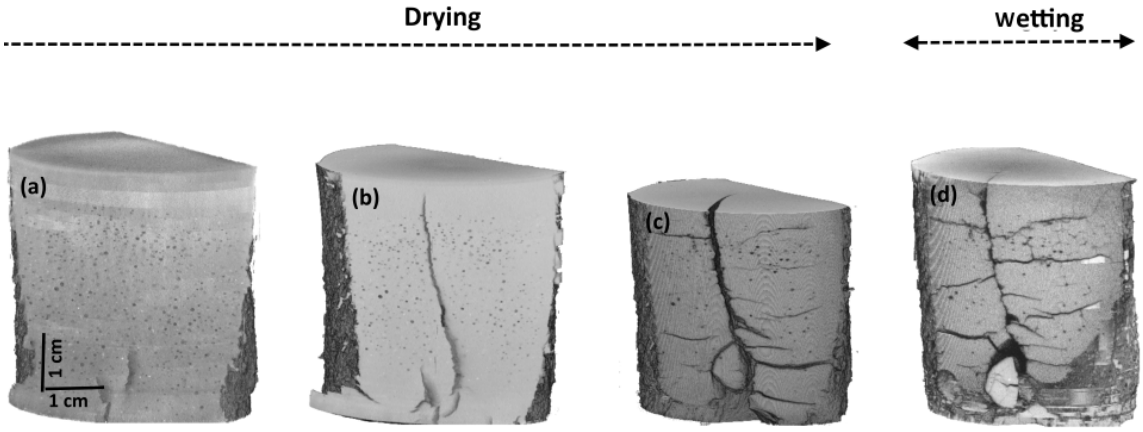

Fig. 9. 3D reconstruction of the soil specimen (cake) during D-W paths at different water content (w): (a) w= 52%, (b) w=35%, (c) w=12%, and (d) w=100% (after 24 h of wetting)

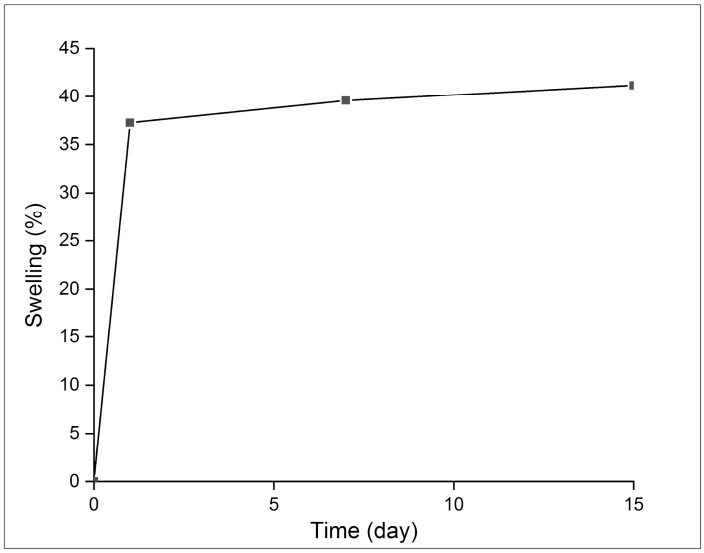

Fig. 10. Global swelling kinetics during wetting path

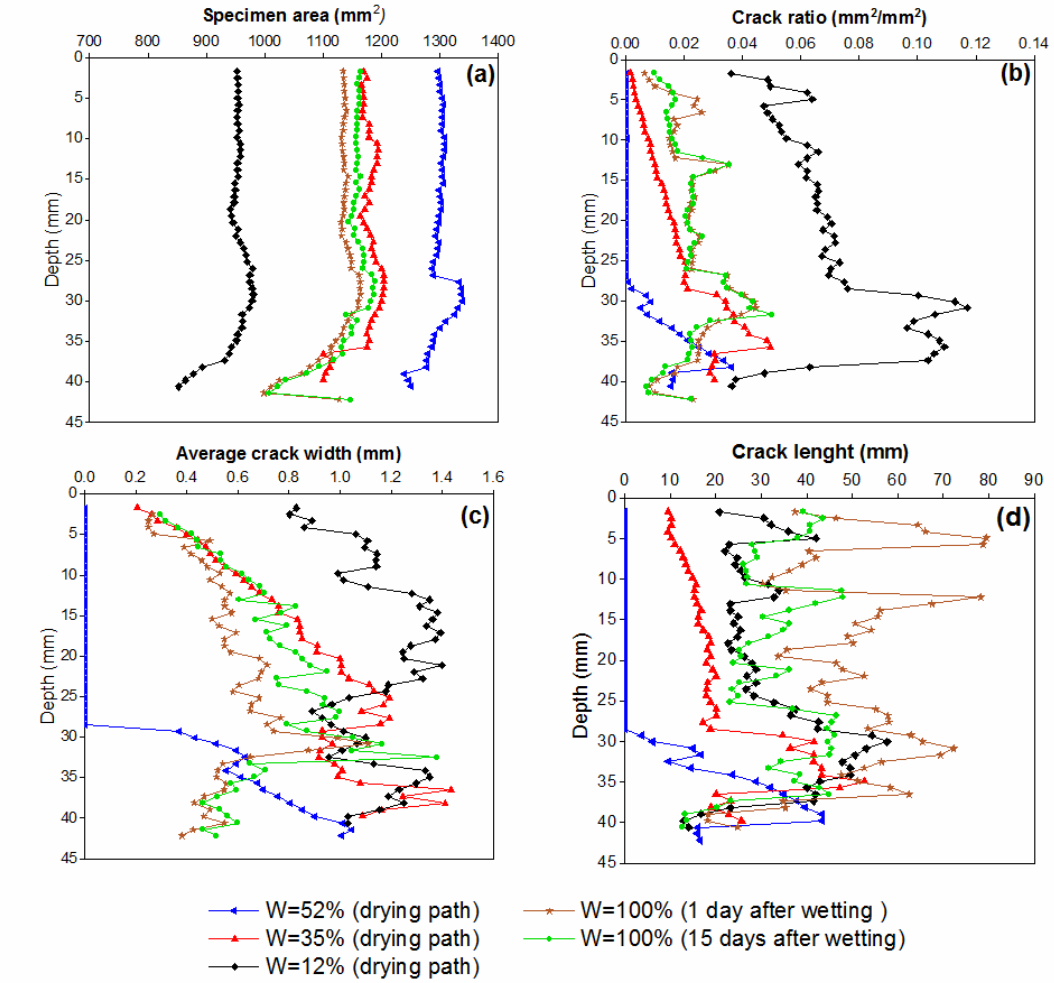

Fig. 11. Evolution of the crack parameters of the soil specimen (cake) during D-W paths. (a) Specimen area, (b) crack ratio, (c) average crack width, and (d) total crack length

Tables

Tab. 1. Properties of the soil

Soil property	**Value**
Density of solid grains (g/cm^3)	2.7
Atterberg limit	
Liquid limit (%)	66
Plastic limit (%)	32
Plasticity index (%)	34
Bulk- rock mineralogy (%)	
Quartz	50
Calcite	20
Dolomite	10
Clay	20
Particle size (µm)	
d_{90}	400
d_{60}	48
d_{50}	25
d_{10}	2.4
Organic matter content MO (%)	3

Tab. 2. Used saturated salt solutions

Salt	Relative Humidity (%)	Suction (MPa)
$CaSO_4$	90.2	13.1
NaCl	75.8	38.1
NH_4,Cl	42.0	113.5
LiCl	12.7	296.4

Graphical abstract